

Nanoconfined Electrochemical Nucleation of Crystalline Molecular Monolayers on Graphite Substrates

Daniel E. Hooks, Christopher M. Yip, and Michael D. Ward*

Department of Chemical Engineering and Materials Science, University of Minnesota, Amundson Hall, 421 Washington Avenue Southeast, Minneapolis, Minnesota 55455

Received: July 2, 1998; In Final Form: September 5, 1998

Real-time in situ atomic force microscopy (AFM) has been employed to examine the electrochemical nucleation of epitaxially oriented, crystalline monolayers of bis(ethylenedithiolo)tetrathiafulvalene triiodide, (ET)₂I₃, on the basal plane of highly oriented pyrolytic graphite electrodes decorated with circular, single-layer-deep pits created by thermal etching. The nucleation of the monolayers in the pits is inhibited compared to the contiguous terraces. The time required for pit filling scales inversely with pit diameter, with nucleation completely suppressed in pits with diameters less than 100 nm. The suppression of growth in the pits can be attributed to the surface discontinuity created by the pit edge that prevents surface diffusion of ET growth units from the surrounding terrace to the pit. Consequently, growth of nuclei in the pits is limited by the amount of ET arriving in the pit by diffusion directly from solution. Numerical simulations of aggregate growth in pits illustrate the influences of transport and the finite boundary created by pit wall on the evolution of aggregate shape and size during growth, while revealing the most probable locations for nucleation within the pit. These studies illustrate the convenience of investigating nucleation processes triggered by electrochemically driven changes in redox state, the advantage of AFM for probing nucleation in the nanoscale-confined environments, and the role of transport in nucleation of ordered films.

Introduction

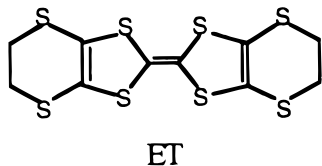
Oriented crystalline molecular films and nanostructures have received considerable attention owing to their technological promise in electronic devices, sensors, displays, and logic elements.¹ Reliable fabrication of these films will depend on the ability to predict and control the structure, morphology, defects, and orientation of these films. Strategies for controlling polymorphism and orientation of thin films have emerged recently, including the use of electric fields² and specific epitaxial relationships between crystalline overlayers and ordered substrates.^{3–6} However, advances in the synthesis of molecular films requires a better understanding of the nucleation events that precede film formation. Determination of critical nucleus dimensions and elucidation of the factors that govern critical size are particularly important for fabricating nanoscale molecular features and controlling domain defects in contiguous molecular films.

The investigation of nucleation processes typically is limited by the inability to characterize, either directly or indirectly, individual events associated with molecular ordering that lead to the formation of stable nuclei. Real-time in situ scanning-probe microscopies have enabled direct visualization of molecular films and their formation, but the initial nucleation events typically must be surmised from the structure and orientation of a mature thin film. Direct visualization of nucleation by scanning-probe microscopy is complicated by the probabilistic and stochastic nature of the process. This frustrates observation of nucleation events on selected substrate regions at desired times and requires numerous observations for meaningful statistical analysis. Furthermore, nucleation must be examined at length scales near the critical dimensions in order to probe molecular ordering precisely.

Recently, the epitaxial ordering of 4'-octyl-4-biphenylcarbonitrile (8CB) liquid crystal monolayers was examined by scanning tunneling microscopy on highly oriented pyrolytic graphite (HOPG) that had been thermally etched to afford well-defined mono- and multilayer pits on the (0001) HOPG basal plane with pit diameters ranging from 5 to 500 nm, depending upon treatment conditions.^{7–10} These pits served as "molecule corrals" that enabled visualization of stochastic ordering in confined areas with a rather simple geometry.¹¹ The number of pits containing ordered monolayers decreased with decreasing pit diameter, and the monolayers appeared disordered in the vicinity of the pit edges, suggesting that the pit edges perturbed ordering of the liquid crystal film. Although the factors responsible for this behavior have not been fully elucidated, the observed behavior may reflect the inability of the monolayers to achieve critical dimensions because of the dimensional constraints of the pit or unfavorable molecular orientations induced by the pit walls that destabilize the ordered film.

Our laboratory recently reported the electrochemical synthesis, on HOPG electrode substrates, of crystalline monolayers based on the charge-transfer salt bis(ethylenedithiolo)tetrathiafulvalene triiodide, (ET)₂I₃.^{12,13} Real-time in situ atomic force microscopy (AFM) revealed that because of epitaxial interactions between the monolayers and the HOPG substrate, monolayer growth initiated by electrochemical oxidation of ET in the presence of triiodide occurred exclusively on pristine terraces instead of at step edges that decorated the HOPG surface. Two monolayer structure types with the same composition were observed, one mimicking the (001) plane of β -(ET)₂I₃ (Type I) and the other resembling a slightly expanded form of the ($\bar{1}10$) plane of β -(ET)₂I₃ (Type II). The Type I and Type II monolayers exhibited azimuthal orientations that reflected coincident epitaxy

with the HOPG substrate, but the aggregation and nucleation processes at initial stages of growth are not understood.



Herein, we describe real-time in situ AFM investigations of the electrochemical nucleation of the Type I and Type II (ET)₂I₃ monolayers in pits on thermally treated HOPG substrates. Electrocrystallization has several advantages with respect to studying nucleation: (i) the ability to trigger nucleation by electrochemically driven changes in redox state provides for accurate measurement of nucleation times from a common reference time (when the electrode potential is switched to the value for ET oxidation), (ii) the solute concentration at the substrate surface can be controlled potentiostatically, (iii) monolayers can be repeatedly grown and removed electrochemically so that a statistically meaningful number of nucleation events within pits of various sizes can be obtained, (iv) the use of dilute solutions of the monolayer components (instead of neat liquids that have been used in the aforementioned liquid crystal studies) eliminates solution-mediated ordering that may bias nucleation statistics. These experiments have revealed that nucleation of both types of (ET)₂I₃ monolayers is substantially inhibited in the pits compared to contiguous terraces, with the time required for nucleation scaling inversely with pit diameter. This behavior can be attributed to the surface discontinuity at the pit edge that prevents surface transport of ET growth units from the surrounding terrace to the pit, thereby restricting aggregate growth to the limited amount of ET that reaches the pit by direct diffusion from solution. Numerical simulations of aggregate growth in pits illustrate the influences of transport and the finite boundary created by the pit wall with respect to the evolution of aggregate shape and size during growth, while revealing the most probable locations for nucleation within the pit.

Experimental Section

Pitted graphite substrates were prepared by placing freshly cleaved highly oriented pyrolytic graphite (HOPG) (Grade ZYA, Advanced Ceramics Corp., Cleveland, OH, 1.2 cm × 1.2 cm × 0.2 cm) in a box furnace preheated to 800 °C. The HOPG substrates were placed in ceramic crucibles prior to heating. The samples were heated in air for approximately 140 s, removed from the furnace, and allowed to cool in the laboratory at ambient temperature. The exposure time and temperature influence the density of pits. Prolonged heat treatment (> 5 min at 800 °C) resulted in an extremely pitted surface structure with large surface cracks that were clearly visible by optical microscopy. The substrates were mounted on steel AFM specimen disks with silver paint (Ted Pella, Inc.).

Electrocrystallization experiments were performed in freshly prepared acetonitrile solutions containing 2 mM tetrabutylammonium triiodide (*n*-Bu₄N⁺I₃⁻) and 0.5 mM bis(ethylenedithio)tetrathiafulvalene (ET, Aldrich). The *n*-Bu₄N⁺I₃⁻ was prepared according to the following procedure. To 120 mL of 1.7 M aqueous solution of potassium iodide (Aldrich) was added 5 g (0.01354 mol) of tetrabutylammonium iodide (Aldrich). To the resulting pale tan solution was added 3.44 g of iodine (Fisher Scientific), affording a dark brown solution with a deep purple oil layer. After the solution was stirred at 70 °C for approximately 10 min, it was allowed to cool to room temperature. The dark black solid was filtered, collected, and rinsed well

with distilled water. Recrystallization from hot methanol and drying in vacuo afforded dark, black shiny platelike crystals of *n*-Bu₄N⁺I₃⁻. Elemental analysis (Galbraith Laboratories) was consistent with the desired triiodide compound.

AFM experiments were performed on a Digital Instruments Nanoscope III MultiMode scanning-probe microscopy system in contact mode using a glass liquid cell (Digital Instruments Inc.), 200 μm Si₃N₄ cantilever tips, and a scanner with a maximum lateral scan range of 15 μm × 15 μm. AFM data was acquired in height, deflection, and lateral force modes for each experiment. The HOPG substrate was used as the working electrode. The width of the HOPG substrates exceeded the diameter of the AFM liquid cell O-ring so that the steel mount did not contact the solution. Platinum counter and (I⁻/I₃⁻/Pt) reference electrodes were fitted to an Y-shaped polypropylene connector inserted into the outlet port of the liquid cell. The reference electrode, consisting of a Pt wire in an acetonitrile solution containing 0.1 M I₂ and 0.05 M *n*-Bu₄N⁺I₃⁻, was contained in a glass tube and separated from the growth solution by a Vycor tip. This electrode had a stable potential of +0.660 V vs Ag/AgCl and was compatible with the acetonitrile electrocrystallization solution. For convenience, electrode potentials are reported herein vs Ag/AgCl. Potentiostatic control was maintained using a Pine AFRDE4 potentiostat, while the cell current was measured with a Keithley 175 digital multimeter. Monolayer growth and dissolution was performed at potentials of +0.650 and +0.350 V vs Ag/AgCl, respectively. The dissolution potential was applied for a period of time sufficient for complete removal of the original monolayer.

Numerical simulations were performed using a Basic code in a Windows 95 environment on a Pentium PC. Both the annotated source code and the compiled Windows 95 program are available for download at <http://www.cems.umn.edu/research/ward/software.html>.

Results and Discussion

Contact-mode AFM imaging of a typical thermally treated HOPG substrate in acetonitrile revealed well-defined circular pits with diameters ranging from 10 to 500 nm. The depth of most pits was 7 Å, equivalent to the *c* lattice parameter and two molecular layers of graphite. Occasionally, 3.5 Å steps were detected, in agreement with the *c*/2 lattice parameter of the HOPG structure. The majority of the pits were circular, although some large noncircular pits were observed that apparently formed by coalescence of growing individual pits during thermal treatment. Lattice images acquired by AFM revealed hexagonal periodicity consistent with the (0001) plane of graphite on both the surrounding terraces and within the pits. Lattice images could not be obtained in pits with diameters < 10 nm owing to resolution limits imposed by the size of the AFM tip.

Formation of β-(ET)₂I₃ monolayers on the pit-decorated HOPG substrates was examined by AFM during application of the growth potential (−0.010 V vs the I⁻/I₃⁻/Pt reference electrode used, equivalent to +0.650 V vs Ag/AgCl). Monolayer formation occurred predominantly on the terraces surrounding the pits, with the pits usually filling in only after the terrace was completely covered by the β-(ET)₂I₃ monolayer (Figure 1). When nucleation did occur in a pit, the pit filled completely on the time scale of image acquisition (ca. 1 min). The actual growth of nuclei in the pit has not been observed. However, the formation of a monolayer in a pit signifies a nucleation event. The inability to observe growth of nuclei within the pits may be due to mechanical perturbation by the AFM tip in the contact imaging mode used here. It is feasible

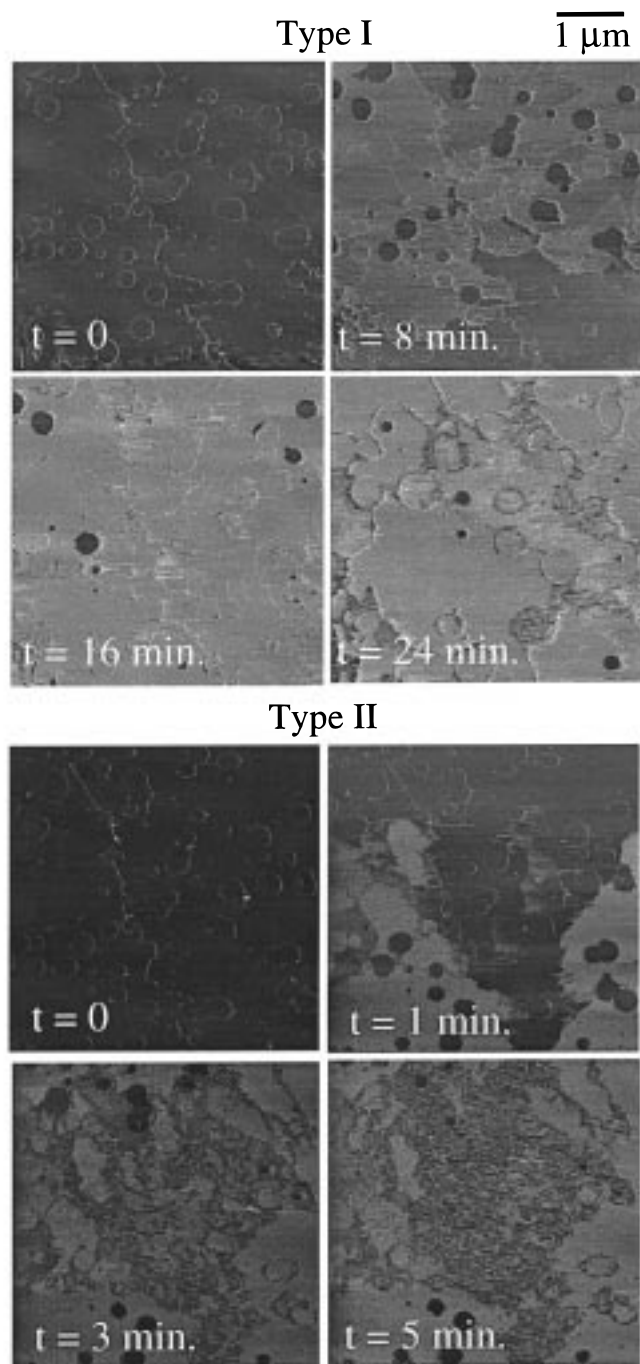


Figure 1. Real-time in situ AFM images acquired during growth of Type I (top) and Type II (bottom) β -(ET) $_2$ I $_3$ monolayers on pitted HOPG electrode substrates. Lateral force images are shown here to depict better the contrast between the monolayer and the HOPG substrate.

that the walls of the pit confer mechanical stability to the monolayer when the pit is completely filled. We are examining this possibility with alternative noncontact imaging modes. Numerous trials indicated that (i) monolayer nucleation was not initiated at pit edges, in agreement with the absence of step-initiated growth on untreated HOPG terraces, (ii) monolayers on the terrace did not induce nucleation in the pit, and (iii) monolayer nucleation within a pit, when it did occur in the absence of terrace growth, did not induce nucleation on the surrounding terrace. Nucleation occurred at different terrace locations and in different pits in successive growth sequences, consistent with random nucleation events and the absence of persistent nucleation centers.

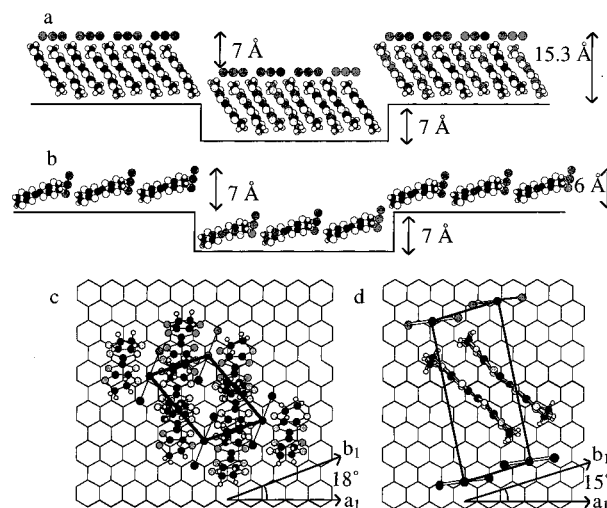


Figure 2. (a) Schematic representation of the (001) β -(ET) $_2$ I $_3$ monolayer (Type I) in a HOPG pit and the surrounding terrace as viewed parallel to the substrate. (b) Schematic representation of the (110) β -(ET) $_2$ I $_3$ monolayer (Type II) in a HOPG pit and the surrounding terrace as viewed parallel to the substrate. (c) Schematic representation of the coincident epitaxial orientation of the Type I monolayers on HOPG, illustrated with a single unit cell of the monolayer. (d) Schematic representation of the coincident epitaxial orientation of the Type II monolayers on HOPG, illustrated with a single unit cell of the monolayer. The layer thicknesses indicated in a and b are based on the (001) and (110) layer thicknesses in the bulk β -(ET) $_2$ I $_3$ crystal, which are nominally identical to the values measured by AFM. The azimuthal orientation of the monolayers, defined by the angle subtended by the HOPG a_1 and monolayer b_1 lattice vectors, is indicated in c and d.

Lattice images acquired by AFM revealed that the monolayers grown in the pits and on the terraces grew as two different structural types that were identical to monolayer structures previously observed on untreated HOPG in our laboratory.^{3c-e} The Type I monolayer exhibited lattice parameters ($b_1 = 6.2$ Å, $b_2 = 9.4$ Å, $\beta = 107^\circ$) and a layer thickness (ca. 15.3 Å) that mimicked the structure of the (001) layers in bulk β -(ET) $_2$ I $_3$ (Figure 2a,c). The Type II monolayer exhibited lattice constants ($b_1 = 7.2$ Å, $b_2 = 17.3$ Å, $\beta = 83^\circ$) and a layer thickness (ca. 6 Å) that were consistent with a slightly expanded form of the (110) plane of β -(ET) $_2$ I $_3$ (Figure 2b,d). Type I monolayers predominated with Type II monolayers forming only occasionally, in agreement with our previous studies. Type II monolayers appear to form more readily following growth and removal of Type I monolayers, but the reasons for the selectivity for Types I and II in a given growth cycle are not understood. The observation of both types on the pitted HOPG substrates provides an opportunity to examine the nucleation behavior of two different monolayers.

The height difference between the monolayers in the pits and on the surrounding terrace for each monolayer type was identical to the height difference between the bare pits and terrace (usually 7 Å). This demonstrates that the monolayers followed the contour of the substrate surface and that the same monolayer type grew in pits and on terraces within a given growth sequence. The latter was confirmed by lattice imaging of the monolayers in the pits and adjacent terraces. Both Type I and Type II monolayers exhibit preferred azimuthal orientations on the HOPG substrate because of coincident epitaxy,¹⁴ which produces three crystallographically and energetically equivalent domain orientations for each monolayer. Consequently, monolayers on the terraces exhibited well-defined grain boundaries due to merging of individual epitaxial crystalline domains.¹⁵ Lattice imaging also revealed that the azimuthal orientation of the

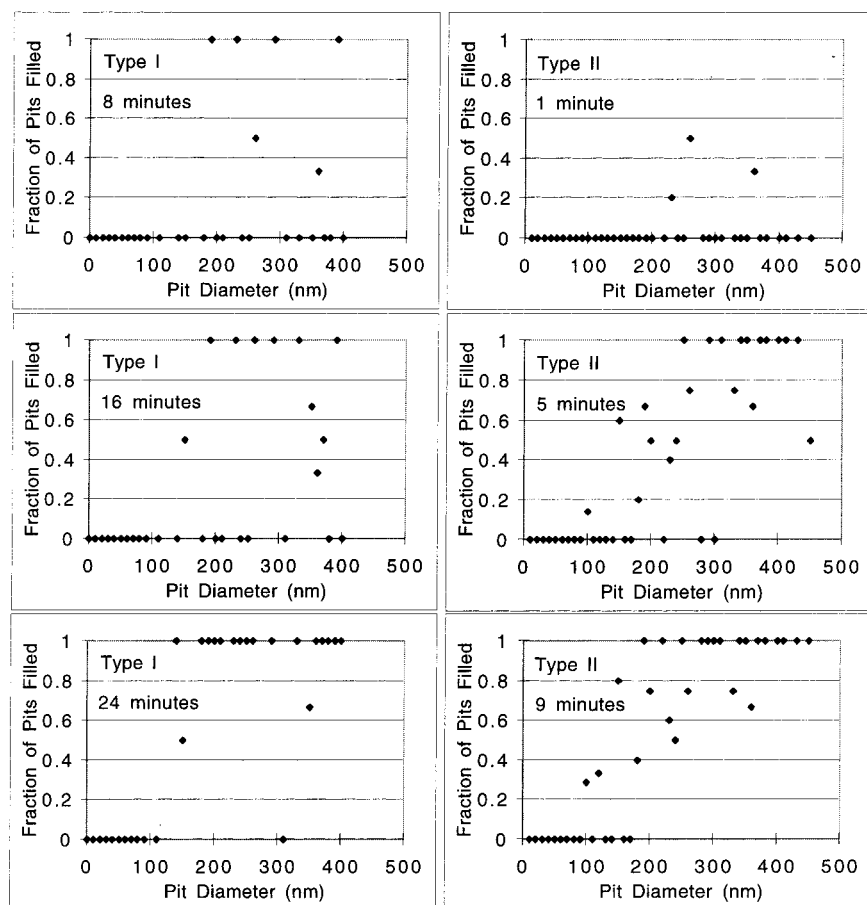


Figure 3. Statistics for monolayer nucleation in various pit sizes for Type I and Type II β -(ET) $_2$ I $_3$ monolayers at times indicated. The data reveal that the fraction of pits filled increases with time and size. Pits with diameters <100 nm remain unfilled within the measured times. Longer measurement times were precluded by the onset of bulk crystallization on top of the monolayers.

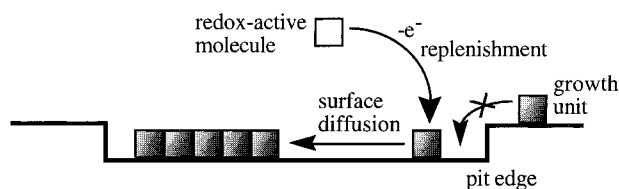
monolayers in the pits was identical to that of the surrounding terrace monolayers only one-third of the time, consistent with a statistical distribution of orientations and the absence of an orientational correlation between pit and terrace monolayers.

The broad distribution of pit sizes on a single HOPG substrate enables simultaneous measurement of monolayer nucleation in different pit sizes, while the ability to repeat the growth sequence by electrochemical removal of grown monolayers enables the acquisition of a statistically meaningful number of measurements. Furthermore, monolayer formation in the pits can be deduced from AFM data without having to obtain molecular-scale contrast, enabling measurements on large substrate areas in a single image frame so that many nucleation events can be recorded simultaneously. Nucleation statistics were compiled for both monolayer types by measuring the fraction of pits filled for differently sized pits at specific times following the application of the monolayer growth potential (Figure 3). Type II monolayers, which have one-half the density and are less thermodynamically stable than Type I monolayers, grew on terraces and within pits approximately twice as fast as Type I layers. This suggested that growth in the substrate pits was significantly influenced by transport. For example, nearly all pits with diameters >100 nm were filled by the Type II monolayer within 10 min, compared to 24 min for the Type I monolayer. In both cases, large pits filled more quickly than small pits, and pits with a diameter <100 nm remained unfilled. *This suggests that the critical radius for the 2-D nuclei is no greater than 50 nm.* Very large pits (diameter > 500 nm) filled as quickly as the surrounding terraces.

Transport-Limited Nucleation Model. Nucleation of a 2-D molecular aggregate on a substrate surface hinges on achieving a critical size at which the probability of continued growth is equivalent to that for dissolution.¹⁶ This size is influenced by several energetic terms, including the energies of the substrate–liquid (γ_{s-l}), monolayer–liquid (γ_{m-l}), and monolayer–substrate (γ_{m-s}), interfaces, and the total volume free energy of the condensed monolayer phase, $4\pi r_{agg}^2 h \Delta G_v$, where r_{agg} , h , and ΔG_v are the radius, height, and specific volume free energy of the 2-D aggregate, respectively. The γ_{m-l} term will actually have multiple components owing to the crystallographic anisotropy of the monolayer and the different energies of the various exposed “faces”. These terms are not directly affected by the pit wall, but the confinement provided by small pits can limit the volume free-energy term to values below that required for stable nuclei. Interactions between the pit edge and the monolayer may also perturb ordering near the edge by inducing nonepitaxial molecular orientations, thereby destabilizing monolayers in pits with diameters near the critical size. Additionally, the growth of an aggregate that initially forms near a pit wall will be physically obstructed along one direction by the wall, slowing the achievement of critical size. These effects all argue that nucleation of a monolayer can be unfavorably perturbed by the proximity of the pit wall.

While these thermodynamic factors may influence the formation of monolayers in the pits, monolayer nucleation and growth also require transport of the redox-active molecules to the electrode surface, where they are oxidized, followed by transport of the growth units to the edge of a growing aggregate by

SCHEME 1



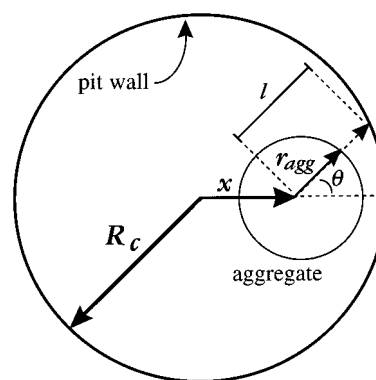
diffusion along the surface (in the case of β -(ET)₂I₃ monolayers, these growth units may be the ET₂⁺ dimer, which constitutes the fundamental unit in the crystal). If growth occurred only by direct attachment of solute molecules from solution to the aggregate edge, nucleation rates on terraces and in pits would be identical (with the possible exception of very small pits for which the edges may influence current distribution). Consequently, the time required for nucleation in pits exceeding the critical size may reflect the *rate* at which ET species reach the advancing boundary of a growing aggregate (Scheme 1).

The observation of suppressed nucleation in pits can be explained by the surface discontinuity created by the pit edge that acts as a barrier to surface diffusion from the terrace to the pit. In order for a growth unit to move from the terrace to the pit, it would need to desorb from the terrace and then re-adsorb in the pit. This process, thus, becomes indistinguishable from adsorption of the growth unit directly from solution. Assuming a circular shape and radially uniform growth vectors for a monolayer aggregate, growth on a terrace will rely on surface diffusion of the growth units to the advancing edge of the aggregate. An aggregate growing on the terrace can draw growth units from the entire terrace by radially symmetric surface diffusion. Therefore, semi-infinite conditions with respect to surface diffusion to the edge of the aggregate can be reasonably assumed, and the $\lim_{x \rightarrow \infty} C_o(x, t) = C_o^*$ can be used as a boundary condition (where C_o^* represents the surface concentration of the growth units). In this case, diffusion to the growing aggregate can be solved analytically with a differential equation, assuming a single moving boundary (the aggregate edge).¹⁷ Growth of an aggregate by surface diffusion under these conditions is unusual in that the growth of the depletion region with time does not affect the concentration gradients near the aggregate edge because the diffusion field draws growth units from a continually larger area, not unlike semi-infinite spherical diffusion.¹⁸

In contrast, the semi-infinite boundary condition cannot be assumed for aggregate growth in a pit. The pit wall serves as a finite boundary because surface diffusion from the surrounding terrace is prohibited by the pit edge. Consequently, the concentration gradient between the edge of a growing aggregate and the wall will be affected by growth of the aggregate, the proximity of the aggregate to the wall, and the flux of redox-active molecules to the pit from solution. This scenario can be described by a differential equation with two changing boundary conditions (the aggregate boundary position and the concentration at the pit wall), which can only be solved numerically.¹⁷

Numerical simulations were performed based on a model in which a nucleation event begins at a radial distance x from the center of a pit with a radius R_c (Scheme 2). The aggregate has a shape described by the vector \mathbf{r}_{agg} , which has a magnitude r_{agg} and a direction θ , the angle between the extension of x and \mathbf{r}_{agg} . It is assumed that the aggregate is initially circular (r_{agg} is uniform with θ) with a radius that we have arbitrarily chosen to be $r_{agg,init} = 1$ nm (this value is approximately the size of an aggregate of two ET molecules packed with the density of the

SCHEME 2



bulk monolayers). An origin is defined at the center of the initial aggregate, and l is defined as the distance from the origin to the pit wall at angle θ , which is given by the positive solutions of eq 1. The simulations are performed by dividing the pit into

$$l = \frac{2x \cos \theta \pm \sqrt{(-2x \cos \theta)^2 - 4(x^2 - R_c^2)}}{2} \quad (1)$$

wedges emanating from a chosen value of x and subtended by arcs ϕ from 1° to 180° (181° to 360° are related by mirror symmetry to these angles in this analysis). Within a wedge, the aggregate occupies an area, A_{int} , described by eq 2.

$$A_{int} = \frac{1}{2} r_{agg}^2 \frac{\phi \pi}{180} \quad (2)$$

Diffusion to the aggregate within each 1° wedge ($\phi = 1^\circ$) can be approximated by linear diffusion along the bisector of the wedge. The concentration, c , along the length, r , can be determined by solving the differential equation (obtained by mass balance) represented by eq 3, using the boundary conditions specified by eqs 3a and 3b, where r is the radial distance from the origin, and c_{surf} is the initial uniform surface concentration. Two integrations and utilization of the boundary conditions

$$0 = \frac{-D_{surf}}{r^2} \frac{d}{dr} r^2 \frac{dc}{dr} \quad (3)$$

$$c = 0 \text{ at } r = r_{agg} \quad (3a)$$

$$c = c_{surf} \text{ at } r = l \quad (3b)$$

yield eq 4. For each angle θ , the flux, J_{surf} , to the outer edge

$$c = \frac{c_{surf} l}{(l - r_{agg})} - \frac{c_{surf} r_{agg}}{r(l - r_{agg})} \quad (4)$$

of the aggregate at $r = r_{agg}$ is given by eq 5, where D_{surf} is the surface diffusion coefficient. The number of molecules, N_m ,

$$J_{surf} = -D_{surf} \frac{dc}{dr} = -D_{surf} \frac{c_{surf} r_{agg} l}{r^2 (l - r_{agg})} = -D_{surf} \frac{c_{surf} l}{r_{agg} (l - r_{agg})} \quad (5)$$

in time increment, t_{inc} , diffusing to the outer edge of the aggregate is given by eq 6, and the new aggregate radius within this wedge after time increment t_{inc} is given by eq 7, where ρ

is the two-dimensional density of the crystalline monolayer. The

$$N_m = J_{\text{surf}} t_{\text{inc}} \left(\frac{2A_{\text{init}}}{r_{\text{agg}}^2} \right) \quad (6)$$

$$r_{\text{agg,new}} = \sqrt{\frac{2(A_{\text{init}} + \frac{N_m}{\rho})}{\frac{\phi\pi}{180}}} \quad (7)$$

corresponding area for the larger aggregate within the wedge after time increment t_{inc} is given by eq 8. The area of the entire

$$A_{\text{init,new}} = \frac{1}{2} r_{\text{agg,new}}^2 \frac{\phi\pi}{180} \quad (8)$$

aggregate after time increment t_{inc} is simply two times the sum of the $A_{\text{init,new}}$ values that were calculated over the range $1^\circ \leq \theta \leq 180^\circ$.

After the first time increment, the area of exposed HOPG (that is, the area uncovered by the monolayer aggregate) with in each wedge and a new growth unit concentration are calculated. The latter is based on the initial surface concentration, the number of molecules consumed during the last time increment, the area left available within each wedge, and the flux of molecules arriving at the surface from solution. The entire process is then repeated for the next time increment and for all values of x (see Appendix). The numerical simulation program uses this algorithm to model aggregate growth in pits of various sizes, providing the aggregate shape and area at different values of x as a function of time. The time increment used in the calculation is chosen based on a compromise of several parameters. The diffusion calculations are most accurate with smaller time increments, but smaller time increments increase the total calculation time. Time increments also must be large enough to allow whole numbers of molecules to reach the exposed substrate regions within each wedge during a simulation cycle. Otherwise, growth in the simulations ceases. This is particularly important when the exposed wedge area becomes very small as the aggregate approaches the pit wall.

The flux of the redox-active solution species to the pit (J_{sol}) can be estimated from experimentally measured electrooxidation currents and the pit sizes (R_c) can be obtained directly from AFM, whereas the surface diffusion (D_{surf}) and the time increment (t_{inc}) are parameters that are adjusted to allow visualization of stepwise aggregate growth while obtaining reasonable agreement between the simulated and experimentally observed times for nucleation in a selected range of pit sizes. The simulations return an aggregate area at selected times. The stability of the 2-D nucleus and, therefore, the probability of nucleation at a given location defined by (x, θ) scales with these areas. However, the number of available nucleation sites for a given value of x increases as $2\pi x$ because of the increasing circumference of the annuli upon which nucleation can occur. At any location x , the unweighted probability of nucleation (P_u^x), which is proportional to the aggregate area at x , must be weighted by $2\pi x$ to account for the increasing number of nucleation sites ($P_w^x = 2\pi x P_u^x$) with x . At a given time t , the most probable annulus for nucleation, which can be denoted as $x_w^{P_{\text{max}}}$, can be determined from the maximum value of the product *aggregate area* $\times 2\pi x$. It is important to note that $x_w^{P_{\text{max}}}$ will differ from the corresponding unweighted quantity $x_u^{P_{\text{max}}}$.

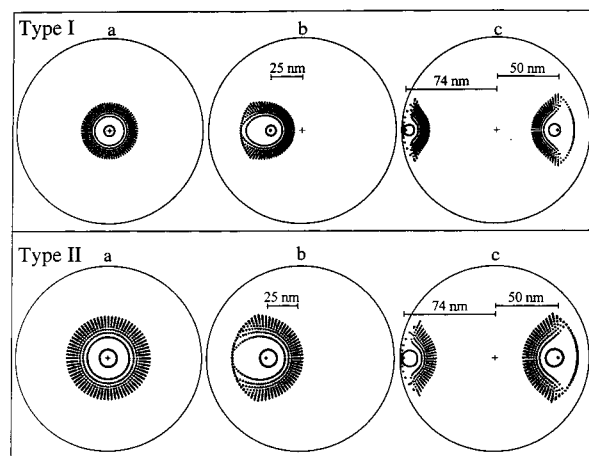


Figure 4. Numerical simulations of 10 generations of Type I (top) and Type II (bottom) aggregate growth in a pit with $R_c = 75$ nm at (a) $x = 0$, (b) $x = 25$, (c) $x = 50$ and 74 nm calculated at time intervals of $t_{\text{inc}} = 1$ s. The first generation depicted in each figure represents growth at $t = 1$ s. The following generations represent successive 1 min intervals. The position at which nucleation was initiated is denoted by the filled dot (●), whereas the center of the pit is denoted by +. The influence of a proximal pit wall is especially evident in b. The aggregate shape of the second generation ($t = 1$ min) is a distorted oval that indicates initially faster growth toward the pit wall, owing to the steeper concentration profile created by the proximity of the pit wall. However, by the second generation ($t = 2$ min), the aggregate advancement toward the edge slows considerably, owing to the decreased number of ET molecules in this region. The ET is depleted because of slow replenishment from solution, the decreasing area of exposed HOPG between the aggregate and the pit wall, and an increasing aggregate edge length that requires an increasing amount of ET in order for the aggregate to advance. The two nucleation and growth events at $x = 50$ and 74 nm depicted in each of the panels (c) are not meant to represent simultaneous events; these are independent simulations combined in one panel here to conserve space. Simulation parameters: $D_{\text{surf}} = 10^{-10}$ cm² s⁻¹; $J_{\text{sol}} = 1.25 \times 10^{-3}$ molecules nm⁻² s⁻¹; $t_{\text{inc}} = 1$ s; $R_c = 75$ nm; $r_{\text{agg,init}} = 1$ nm; $\rho = 3.0$ molecules nm⁻² for Type I; $\rho = 1.5$ molecules nm⁻² for Type II.

Simulation of (ET)₂I₃ Nucleation in Pits. Nucleation events and growth of nuclei in pits were simulated with a program utilizing this algorithm.¹⁹ The time t needed to fill a pit of size R_c can be extracted from the statistical analysis of monolayer growth data. For example, 9 min is required to fill the pits of $R_c \geq 75$ nm with a Type II monolayer (Figure 3). The measured steady-state current of 20 nA at the working HOPG electrode (electrode area = 0.5 cm²) is equivalent to a replenishment flux from solution of 1.25×10^{-3} molecules nm⁻² s⁻¹. The surface diffusion coefficient was assigned a value of 10^{-10} cm² s⁻¹. This value was chosen because it enabled us to discern the evolution of aggregate shape and area in the simulation within time scales similar to that of the pit filling observed experimentally. The densities assigned to the two-dimensional Type I and Type II β -(ET)₂I₃ crystals were $\rho_I = 3.0$ and $\rho_{II} = 1.5$ molecules nm⁻². Successive generations of aggregate growth were calculated at 1 s intervals ($t_{\text{inc}} = 1$ s).

The simulations of aggregate shape and area using these parameters demonstrate how the growth of the aggregate in the pit is influenced by the proximity of the pit wall (Figure 4). As the aggregate edge advances toward the pit wall in the initial stages of growth, the flux and growth actually increases because of the steeper concentration profile imparted by the proximity of the wall. However, aggregate advancement toward the edge slows considerably in following generations owing to the depletion of ET molecules in this region.

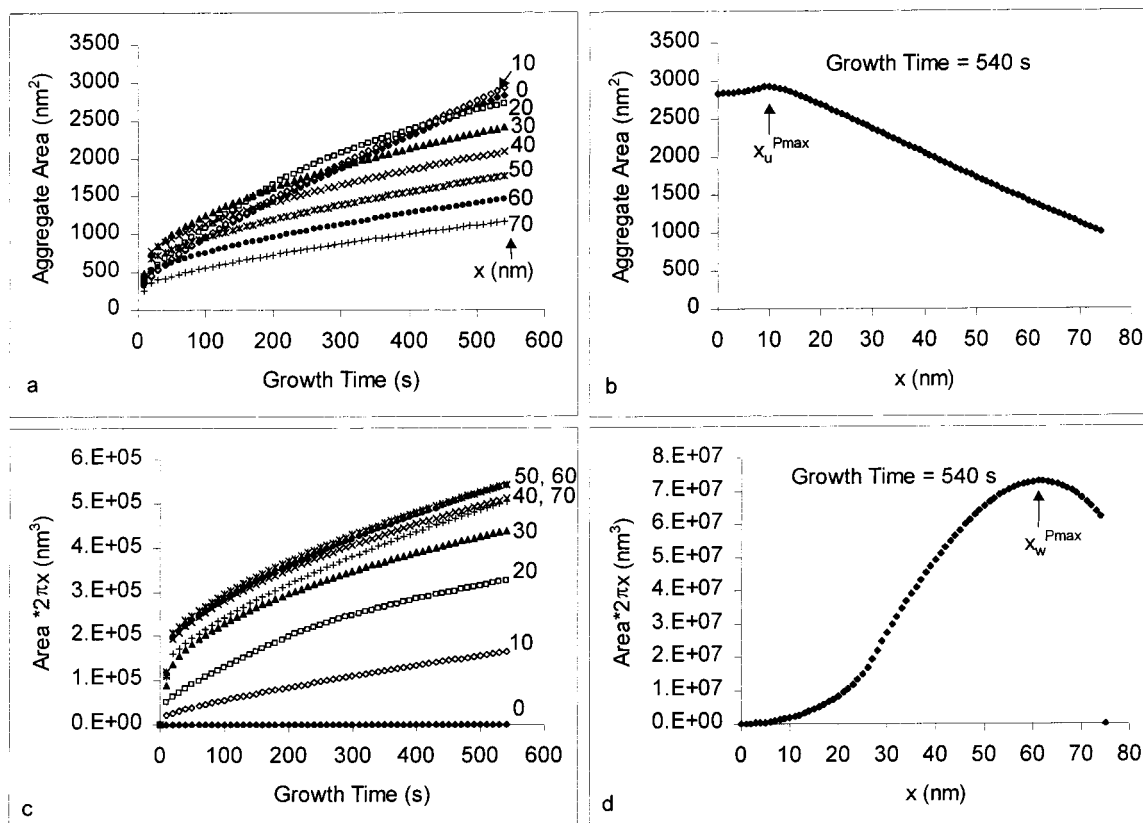


Figure 5. (a) Simulation results for a Type II monolayer depicting the change in aggregate area during growth for various positions, x , at which nucleation is initiated. (b) Dependence of the aggregate area, measured at $t = 540$ s, on x . The maximum at $x = 10$ nm illustrates the influence of the steeper concentration profile on the side of the aggregate closer to the pit wall, which increases the flux of ET to the aggregate edge and a slightly larger area at 540 s. (c) Weighted aggregate area, obtained by multiplying the data in a by $2\pi x$ to account for the increasing number of nucleation sites with increasing distance from the center of the pit. (d) Dependence of the weighted aggregate area on x at $t = 540$ s. The maximum near 60 nm represents the annulus on which nucleation is most probable. Simulation parameters: $D_{\text{surf}} = 10^{-10}$ cm² s⁻¹; $J_{\text{sol}} = 1.25 \times 10^{-3}$ molecules nm⁻² s⁻¹; $t_{\text{inc}} = 1$ s; $R_c = 75$ nm; $\rho = 1.5$ molecules nm⁻².

This depletion is a consequence of slow replenishment of ET in this region due to limiting diffusion from solution and the decrease in electroactive HOPG area that accompanies aggregate growth. Furthermore, the increasing edge length of a growing aggregate requires an increasing number of ET growth units in order for the aggregate to advance along a given direction. The simulations predict that, for a given time, the aggregate area for Type II monolayers is nearly twice that of Type I monolayers. This difference can be attributed to the smaller density of Type II monolayers. Interestingly, the experimental data indicate that the Type II monolayer fills the pits approximately 2 times faster than Type I. The agreement of the simulations with the experimental observations strongly suggests that nucleation and pit filling is a transport-limited process.

The simulations also indicate that nucleation events beginning at different values of x exhibit different aggregate growth rates which, as mentioned above, change further as the aggregate grows. The aggregate actually grows faster if nucleation is initiated at a slight offset from the pit center owing to the steeper concentration profile created on one side of the aggregate by the proximity of the pit wall. The compiled simulation results for a Type II monolayer depicted in Figure 5, with $R_c = 75$ nm, reveal a maximum aggregate size of 3000 nm² after 540 s at $x = 10$ nm. Assuming that the stability of the 2-D nucleus is proportional to its area, this value represents the location, $x_u^{P_{\text{max}}}$, at which the unweighted probability for nucleation reaches a maximum. Multiplying the data in Figure 5b by $2\pi x$ to weight the aggregate areas to the site density of each annulus defined

by x , the largest *weighted* area at 9 min is observed at $x_w^{P_{\text{max}}} = 60$ nm with an aggregate area of 1300 nm². This value of x represents the most probable *annulus* for nucleation at this growth time. The simulations for the Type I monolayers indicate that the largest weighted area at 9 min also occurs at $x = 60$ nm, but with an unweighted area of 2700 nm². The larger area reflects the smaller density of the Type I monolayer ($\rho_I/\rho_{II} = 0.5$); under transport-limiting conditions, the area of Type I monolayers should be twice that of Type II for equivalent growth times and flux.

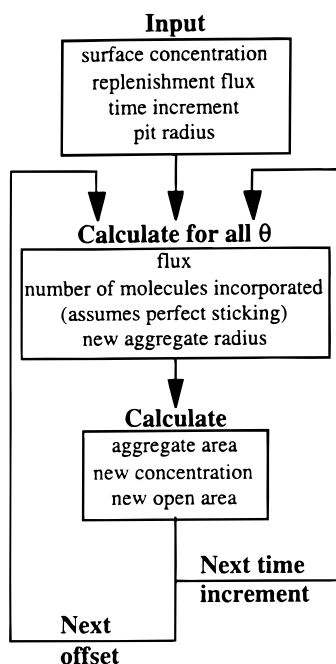
Conclusions

These studies reveal that the nucleation of crystalline organic β -(ET)₂I₃ monolayers, known to grow epitaxially on HOPG, is significantly suppressed in nanoscale pits on HOPG substrates. While the confinement of growth within the pits can frustrate nucleation by preventing the achievement of critical dimensions, the influence of pit size can also be explained by hindered surface transport of ET growth units from the surrounding terrace across the discontinuity introduced by the pit edge. This creates a finite boundary within the pit that affects the concentration gradients and substantially limits the amount of ET available for aggregate growth. Numerical simulations based on transport-limited growth provide insight into the evolution of aggregate shape and area within the pits. While simulations can be sensitive to parameters such as surface diffusion coefficients, the good correspondence of the simulated and experimentally observed times for nucleation, as surmised from

pit-filling events, strongly suggests that nucleation of the β -(ET)₂I₃ monolayers is controlled by transport. The observation of this phenomena is made possible by the finite boundary created by the walls of the nanoscale pit, demonstrating the value of examining molecular assembly processes in nanoscale environments.

Acknowledgment. The authors gratefully acknowledge financial support from the Office of Naval Research.

Appendix. Schematic representation of the algorithm used for numerical simulations of aggregate growth in HOPG pits.



References and Notes

- (1) Aviram, A.; Ratner, M. A. *Chem. Phys. Lett.* **1974**, 29, 277. (b) *Molecular Electronic Devices*; Carter, F. L., Ed.; Marcel Dekker: New York, 1982. (c) *Molecular Electronics*; Ashwell, G. J., Ed.; John Wiley & Sons: New York, 1992. (d) Hillier, A. C.; Schott, J. H.; Ward, M. D. *Adv. Mater.* **1995**, 7 (4), 409.

- (2) Liu, C.-y.; Lynch, V.; Bard, A. J. *Chem. Mater.* **1997**, 9, 943.
- (3) (a) Schott, J. H.; Ward, M. D. *J. Am. Chem. Soc.* **1994**, 116, 6806. (b) Schott, J. H.; Yip, C. M.; Ward, M. D. *Langmuir* **1995**, 11, 177. (c) Hillier, A. C.; Maxson, J. B.; Ward, M. D. *Chem. Mater.* **1994**, 6, 2222. (d) Last, J. A.; Hillier, A. C.; Hooks, D. E.; Maxson, J. B.; Ward, M. D. *Chem Mater.* **1998**, 10 (1), 422. (e) Hillier, A. C.; Ward, M. D. *Phys. Rev. B* **1996**, 54, 14037.
- (4) (a) Forrest, S. R.; Zhang, Y. *Phys. Rev. B* **1994**, 49, 11297. (b) Zhang, Y.; Forrest, S. R. *Phys. Rev. Lett.* **1993**, 71, 2765.
- (5) (a) Collins, G. E.; Nebesny, K. W.; England, C. D.; Chau, L.; Lee, P. A.; Parkinson, B.; Fernando, Q.; Armstrong, N. R. *J. Vac. Sci. Technol. A* **1992**, 10, 2902. (b) Armstrong, N. R.; Nebesny, K. W.; Collins, G. E.; Chau, L.-K.; Lee, P. A.; England, C. D.; Diehl, D.; Douskey, M.; Parkinson, B. *Thin Solid Films* **1992**, 216, 90. (c) Nebesny, K. W.; Collins, G. E.; Lee, P. A.; Chau, L.-K.; Danziger, J.; Osburn, E.; Armstrong, N. R. *Chem. Mater.* **1991**, 3, 829.
- (6) (a) Ludwig, C.; Gompf, B.; Flatz, W.; Peterson, J.; Eisenmenger, W.; Mobus, M.; Zimmermann, U.; Karl, N. Z. *Phys. B* **1992**, 86, 397. (b) Ludwig, C.; Gompf, B.; Peterson, J.; Strohmaier, R.; Eisenmenger, W. Z. *Phys. B* **1993**, 93, 365.
- (7) (a) Evans, E. L.; Griffiths, R. J. M.; Thomas, J. M. *Science* **1970**, 171, 174. (b) Yang, R. T.; Wong, C. J. *Chem. Phys.* **1981**, 75 (9), 4471.
- (8) Yang, R. T.; Wong, C. *Science* **1981**, 214, 437.
- (9) Wong, C.; Yang, R. T.; Halpern, B. L. *J. Chem. Phys.* **1983**, 78 (6), 3325.
- (10) (a) Chu, X.; Schmidt, L. D. *Carbon* **1991**, 29, 9 (8), 1251. (b) Chang, H.; Bard, A. J. *J. Am. Chem. Soc.* **1990**, 112, 4598.
- (11) (a) Patrick, D. L.; Cee, V. J.; Beebe, T. P., Jr. *Science* **1994**, 265, 231. (b) Patrick, D. L.; Cee, V. J.; Beebe, T. P., Jr. *J. Phys. Chem.* **1996**, 100, 8478. (c) Patrick, D. L.; Cee, V. J.; Purcell, T. J.; Beebe, T. P., Jr. *Langmuir* **1996**, 12, 1830.
- (12) (a) Last, J. A.; Hillier, A. C.; Hooks, D. E.; Maxson, J. B.; Ward, M. D. *Chem. Mater.* **1998**, 10 (1), 422. (b) Hillier, A. C.; Maxson, J. B.; Ward, M. D. *Chem. Mater.* **1994**, 6, 2222. (c) Hillier, A. C.; Maxson, J. B.; Ward, M. D. *Chem. Mater.* **1994**, 6, 2222.
- (13) Wang, H. H.; Montgomery, L. K.; Husting, C. A.; Vogt, B. A.; Williams, J. M.; Budz, S. M.; Lowry, M. J.; Carlson, K. D.; Kwok, M.-K.; Mikheyev, V. *Chem. Mater.* **1989**, 1, 484.
- (14) The azimuthal orientation, defined by the angle subtended by the HOPG **a**₁ and monolayer **b**₁ lattice vectors, was measured by comparison of the AFM lattice image of the monolayer with that of the underlying HOPG substrate. The Type I and Type II β -(ET)₂I₃ monolayers exhibit azimuthal angles of 18° and 15°, respectively, which represent coincident orientations for these monolayers (see refs 3c–e).
- (15) Last, J. A.; Ward, M. D. *Adv. Mater.* **1996**, 8, 730.
- (16) Ickert, L.; Schneider, H. G. In *Advances in Epitaxy and Endotaxy*; Schneider, H. G., Ruth, V., Kormany, T., Eds.; Elsevier: Amsterdam, 1990; p 229.
- (17) Crank, J. *Mathematics of Diffusion*, 2nd ed.; Oxford University Press: London, 1975.
- (18) Bard, A. J.; Faulkner, L. R. *Electrochemical Methods: Fundamentals and Applications*; John Wiley & Sons: New York, 1980; p 145.
- (19) The compiled program and source code are available for download at <http://www.cems.umn.edu/research/ward>.